

# Design and fabrication of three-dimensional single-mode waveguide arrays in bulk diamond through direct focused proton beam implantation

Jintao Gong<sup>a,\*</sup>, Kambiz Ansari<sup>b</sup>, Jeroen Anton van Kan<sup>a</sup>

<sup>a</sup> Centre for Ion Beam Applications, Department of Physics, National University of Singapore, 117542, Singapore

<sup>b</sup> Ila Technologies Pte Ltd, 17 Tukang Innovation Drive, 618300, Singapore

## ARTICLE INFO

### Keywords:

3D diamond waveguide arrays  
Ion implantation  
Proton beam writing  
SRIM simulation  
FDE simulation

## ABSTRACT

We demonstrate the feasibility of creating three-dimensional photonic devices through the realization of multi-level waveguides inside diamond by a series of systematic combined simulations grounded on Monte-Carlo statistics and Maxwell solver algorithms. Further, we have fabricated the counterparts of the multi-level waveguides buried in single crystalline diamond using a process based on several proton beam irradiation steps with different energies and fluences. On top of that, we draw a thorough comparison between the simulation results and the experimental observations, and find that they are in a good agreement with each other. Moreover, the simulation results also provide additional information such as the working fluence range of single-mode light (1550 nm) wave-guiding, the effective refractive index, and the polarization direction. The proof-of-concept of producing three-dimensional optical and photonic structures by direct focused proton beam implantation would open up a variety of new opportunities in designing and fabricating optical modulators, photonic components and quantum-computing related functional devices in bulk diamond, thus further promoting the development of three-dimensional diamond photonics.

## 1. Introduction

Achieving complex three-dimensional (3D) structures in a wide spectrum of material systems is crucial to many emerging micro/nano technologies. Varieties of latest technologies such as 3D memory production [1], 3D silicon based photonic component fabrication [2], and 3D non-linear photonic crystal formation [3] have been recently investigated to break present limitations of planar micro/nano photonics. As a matter of fact, 3D multi-layer architectures would reduce restrictions by eliminating horizontal structural overlap by means of vertically stacking as well as overcome the conventional barrier of limited physical chip area. Moreover, 3D multi-level photonics would also offer researchers another dimension to process, thus enabling photonic devices with denser and more complex networks. On the other hand, single crystalline diamond (SCD) inherently provides many excellent properties for optical, photonic and quantum-computing applications. Owing to wide light transmission window and comparatively high refractive index, it is appealing to employ SCD to manufacture light-guiding structures working at wavelengths ranging from ultraviolet (UV) to infrared (IR) [4]. Apart from that, taking advantage of the fact that SCD possesses a wide electronic band-gap and high thermal

conductivity, it can be applied in non-linear nano-photonics fields that require intense laser power and low multi-photon absorption.

Furthermore, it was reported that there exist over five hundred optically active color centers in SCD [5]. Some of these centers are recognized as bright single-photon sources with remarkable coherence and nuclear spin properties, suggesting SCD is a competitive candidate that can be exploited in micro-fluidic networks, quantum optics, quantum computing and quantum information processing applications [6–10]. Nevertheless, being short of high-quality, commercially available and large-scale diamond-on-substrate chips with applicable diamond layer thickness, makes the fabrication of waveguides in SCD challenging. Therefore, to accomplish light confinement in photonic devices, researchers have come up with bonding diamond thin film (tens of micrometers) to a substrate with lower refractive index and subsequently processing the diamond thin film by dry etching [11]. Additionally, considerable efforts have also been devoted into creating light-guiding structures directly on or in bulk SCD, including focused ion beam milling [12], quasi-isotropic dry etching [13], femto-second laser writing [14,15], and Faraday cage based angled etching [16]. The drawback of the above-mentioned methods is that none of them are capable of directly producing 3D multi-level light-guiding structures in

\* Corresponding author.

E-mail address: [e0015115@u.nus.edu](mailto:e0015115@u.nus.edu) (J. Gong).

<https://doi.org/10.1016/j.optmat.2019.109527>

Received 26 September 2019; Received in revised form 25 October 2019; Accepted 9 November 2019

0925-3467/© 2019 Elsevier B.V. All rights reserved.

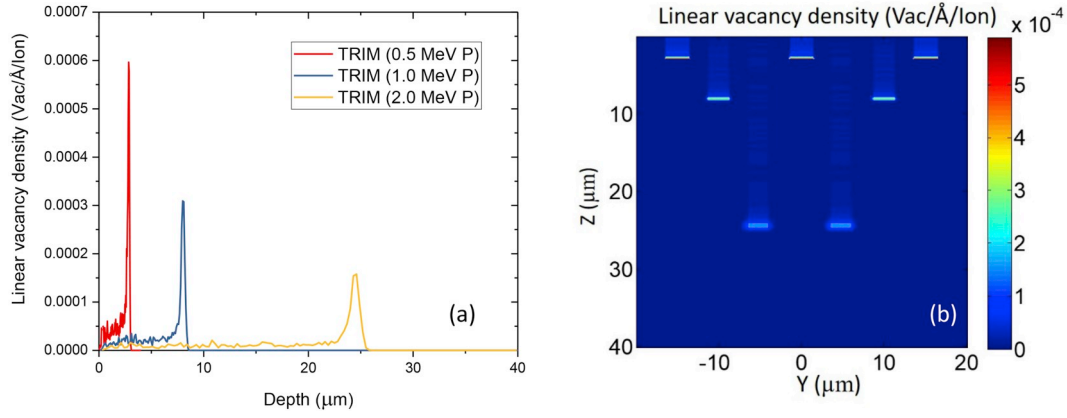


**Fig. 1.** TRIM simulations: (a) proton-implanted linear vacancy distribution profiles of three different incidence energies along the penetrating path in SCD. (b) YZ plane map of 3D waveguide arrays in SCD in terms of linear vacancy density induced by proton implantations.

bulk SCD.

For comparison, we use an alternative powerful technique, namely proton beam writing [17], to create wave-guiding structures in bulk SCD and extend these structures from a plane to a 3D volume in a manner of locally modifying complex refractive index ( $\tilde{n}$ ) of SCD bulk using multiple proton beam energies. Incidentally, it is worth noting that this 3D structuring technique can also be exploited for the fabrication of graphitic conductive channels which are indispensable for the realization of ionizing radiation detectors, infrared radiation emitters and field emitters [18–21]. Specifically, previous research studies [22–24] have found that a proportional increasing of  $\tilde{n}$ , in both real and imaginary parts, of SCD occurs via proton beam implantation. Therefore, by modulating the refractive index with precise spatial control and accurate alteration via proton implantation induced damage, the focused proton beam implantation technique can enable a highly versatile and flexible way of manufacturing 3D quantum-optical and photonic devices in bulk diamond.

## 2. Simulations

### 2.1. The stopping and range of ions in matter (SRIM)

SRIM [25] is a group of Monte-Carlo based computer programs, which can be used for calculating interaction of fast ions with matter. The core of SRIM is a program named Transport of Ions in Matter (TRIM). Considering the advantages of TRIM in calculating penetration

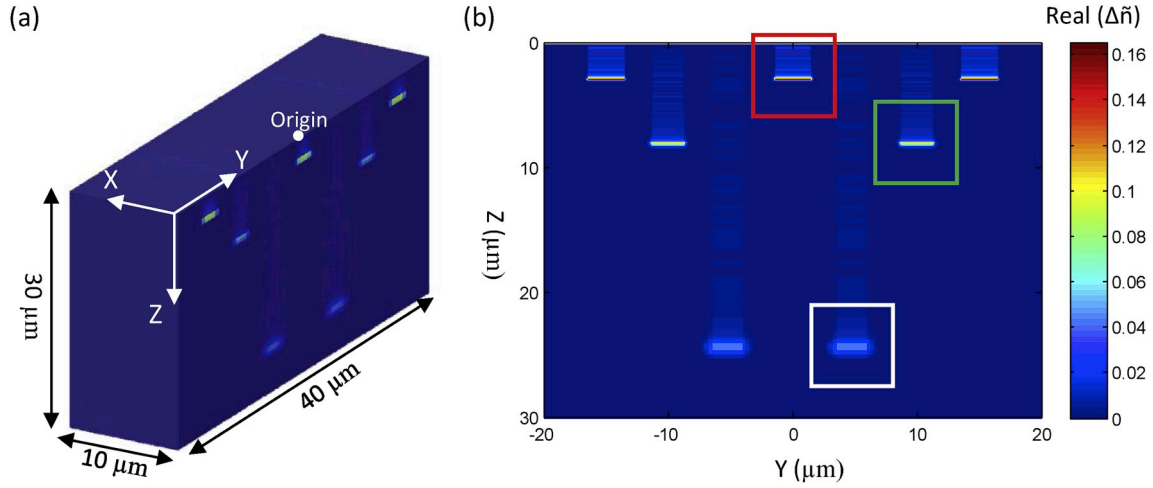
depth, lateral and longitudinal straggling, and induced linear vacancy density, there is no doubt it is a powerful tool in simulating the damage profiles in terms of vacancies created. The reason to choose vacancy distribution to represent the damage profiles is because previous studies [22–24] have identified a linear dependence between complex refractive index and spatial vacancy density, which will be discussed in detail later. Typical diamond parameters used in the TRIM simulations: density 3.515 g/cm<sup>3</sup>, lattice binding energy 3 eV, surface binding energy 7.41 eV, and carbon atom displacement energy 35 eV [26,27].

Fig. 1(a) illustrates the linear vacancy distribution of proton-implanted SCD calculated by TRIM. It consists of three different incidence energies. They are 2 MeV proton, 1 MeV proton, and 0.5 MeV proton, respectively. This was also the implanting sequence of our proton beam writing experiment. As shown in Fig. 1(a), we can see the three Bragg peaks are vertically separated, and the linear vacancy density at a Bragg peak decreases with the increase of the incidence energy. Fig. 1(b) shows a map of linear vacancy density profiles of proton-implanted SCD based on Fig. 1(a), matching our experiments. It comprises seven waveguide channels, a center-to-center distance of 5  $\mu\text{m}$  between each two neighboring channels from the top view (XY plane). The bottom two waveguides were implanted by 2 MeV proton with a center-to-center distance of 10  $\mu\text{m}$ ; the middle two waveguides were formed by 1 MeV proton with 20  $\mu\text{m}$  center-to-center separation; and the top three waveguides were constructed by 0.5 MeV proton with a center-to-center separation of 15  $\mu\text{m}$  between two adjacent waveguides. Every single waveguide channel had a 2  $\mu\text{m}$  beam scan width

**Table 1**

Effective refractive index and polarization vs. proton energy and fluence (2  $\mu\text{m}$  scan size + beam spot size + lateral straggling).

Energy (MeV)			0.5		1		2	
$F_n (\times 10^{15} \text{cm}^{-2})$			$n_{\text{eff}}$	$f_{E_y}$	$n_{\text{eff}}$	$f_{E_y}$	$n_{\text{eff}}$	$f_{E_y}$
$F_1$	2	Mode 1 (M1)	N.A.	N.A.	N.A.	N.A.	N.A.	N.A.
		Mode 2 (M2)	N.A.	N.A.	N.A.	N.A.	N.A.	N.A.
$F_2$	5	Mode 1 (M1)	2.3902 + i0.0152	0 ( $E_x$ )	2.3882 + i0.0123	0 ( $E_x$ )	2.3899 + i0.0108	1 ( $E_y$ )
		Mode 2 (M2)	2.3896 + i0.0161	1 ( $E_y$ )	2.3880 + i0.0127	1 ( $E_y$ )	2.3899 + i0.0107	0 ( $E_x$ )
$F_3$	8	Mode 1 (M1)	2.3976 + i0.0323	0 ( $E_x$ )	2.3947 + i0.0280	0 ( $E_x$ )	2.3965 + i0.0223	1 ( $E_y$ )
		Mode 2 (M2)	2.3961 + i0.0365	1 ( $E_y$ )	2.3944 + i0.0299	1 ( $E_y$ )	2.3965 + i0.0220	0 ( $E_x$ )
$F_4$	10	Mode 1 (M1)	2.4042 + i0.0459	0 ( $E_x$ )	2.4008 + i0.0399	0 ( $E_x$ )	2.4019 + i0.0304	1 ( $E_y$ )
		Mode 2 (M2)	2.4025 + i0.0534	1 ( $E_y$ )	2.4006 + i0.0429	1 ( $E_y$ )	2.4019 + i0.0299	0 ( $E_x$ )
		Mode 3 (M3)	N.A.	N.A.	2.3879 + i0.0052	0 ( $E_x$ )	N.A.	N.A.
$F_5$	15	Mode 1 (M1)	2.4255 + i0.0841	0 ( $E_x$ )	2.4208 + i0.0795	1 ( $E_y$ )	2.4178 + i0.0517	1 ( $E_y$ )
		Mode 2 (M2)	2.4242 + i0.1035	1 ( $E_y$ )	2.4201 + i0.0725	0 ( $E_x$ )	2.4175 + i0.0507	0 ( $E_x$ )
		Mode 3 (M3)	2.3968 + i0.0789	0 ( $E_x$ )	2.3904 + i0.0082	0 ( $E_x$ )	2.3907 + i0.0430	1 ( $E_y$ )
		Mode 4 (M4)	N.A.	N.A.	N.A.	N.A.	2.3906 + i0.0423	0 ( $E_x$ )
		Mode 5 (M5)	N.A.	N.A.	N.A.	N.A.	2.3884 + i0.0071	0 ( $E_x$ )



**Fig. 2.** FDE simulations: (a) spatial distribution of complex refractive index of the multi-energy proton implanted SCD with a volume of  $10 \times 40 \times 30 \mu\text{m}^3$ . (b) YZ plane map ( $40 \times 30 \mu\text{m}^2$ ): three  $8 \times 8 \mu\text{m}^2$  simulation regions are centered at one 0.5 MeV proton implantation formed waveguide channel (marked by a red box), one 1 MeV proton implanted waveguide channel (marked by a green box), and one 2 MeV proton based waveguide channel (marked by a white box), respectively. (For interpretation of the references to color in this figure legend, the reader is referred to the Web version of this article.)

plus corresponding beam spot sizes (see Section 3. Experimental) and its own lateral straggling as calculated by TRIM. Considering proton-implanted complex refractive index modification of SCD is proportional to spatial vacancy density, such a map will be of paramount importance for the following finite element based Maxwell electromagnetic field solvers to perform further light wave-guiding related simulations.

## 2.2. Finite difference eigenmode (FDE)

The FDE simulation is a Maxwell solver directed at calculating mode field profiles and effective refractive index on a cross-section mesh of the waveguide. The finite difference algorithm based on Zhu and Brown [28] is the current method used for meshing the waveguide geometry, and it is capable of accommodating arbitrary waveguide structures. The complex refractive index of bulk pristine diamond at 1550 nm is  $2.3878 + i0.0000$  referring to the database [29], and the relations between the modification of the complex refractive index  $\Delta\tilde{n}$  and the induced vacancy density of SCD were reported in several papers [22–24,30–32]. Among them a typical modeled dependence relation [24] is used in this paper:

$$\Delta\tilde{n} = (3.5 + i3.2) \times 10^{-22} \frac{dN(\text{Vac})}{dV(\text{cm}^3)}. \quad (1)$$

To put it more intuitively, we can rewrite Eq. (1) as

$$\Delta\tilde{n} = (3.5 + i3.2) \times 10^{-14} \left[ F_n \left( \frac{\text{ion}}{\text{cm}^2} \right) \cdot \rho_z \left( \frac{\text{Vac}}{\text{ion} \cdot \text{\AA}} \right) \right], \quad (2)$$

where  $\rho_z$  represents linear vacancy density calculated by TRIM (more specifically, it is a linear vacancy density along the penetrating direction);  $F_n$  ( $n = 1, 2, 3, 4, 5$ ) denotes different fluences (see Table 1). It is worth noting that such a linear dependency between  $\Delta\tilde{n}$  and spatial vacancy density holds provided the spatial vacancy density does not exceed  $\sim 3 \times 10^{21} \text{ Vac}/\text{cm}^3$  [32]. The highest spatial vacancy density is  $\sim 9 \times 10^{20} \text{ Vac}/\text{cm}^3$  when the largest fluence  $F_5$  ( $1.5 \times 10^{16} \text{ cm}^{-2}$ ) is applied for 0.5 MeV proton implantation, which is less than the threshold. Therefore, equipped with the conversion formula, we constructed a block of diamond ( $X \times Y \times Z$ :  $10 \times 40 \times 30 \mu\text{m}^3$ ) in the form of its spatial complex refractive index as shown in Fig. 2(a), which was based on the fluence  $F_3$  ( $8 \times 10^{15} \text{ cm}^{-2}$ ).

Since the block was rendered with scaled colors, it made no difference to display the other four diamond blocks of varying refractive

indexes for the different fluences. Taking advantage of symmetry, the origin was set in the center of the top edge of the front face of the diamond block, as marked in Fig. 2(a). Consequently, the ranges of  $x, y, z$  were  $(0, 10)$ ,  $(-20, 20)$ ,  $(0, 30)$  in the unit of  $\mu\text{m}$ , respectively. Furthermore, the red, green, white boxes in Fig. 2(b) signified the FDE simulated region, they were 2D x-normal planes with an area of  $8 \times 8 \mu\text{m}^2$ . The central position ( $y, z$ ) of the red box was  $(0, 2.8)$ , which was used for calculating mode profiles of 0.5 MeV proton implanted waveguide. Similarly, the center of the green box was  $(10, 8.0)$  and the center of the white box was  $(5, 24.5)$ , aiming to calculate mode profiles of waveguide channels caused by 1 MeV proton implantation and 2 MeV proton implantation, respectively. Furthermore, perfect electric conductor (PEC) boundary conditions were used in all the three FDE simulations.

Specifically, in the x-normal eigenmode solver simulation as shown in Fig. 2(b), we have the vector fields of  $E(y, z)e^{i(-\omega t + \beta x)}$  and  $H(y, z)e^{i(-\omega t + \beta x)}$ , where  $\omega$  is the angular frequency and  $\beta$  is the propagation constant. Then the modal effective refractive index is defined as

$$n_{\text{eff}} = \frac{c\beta}{\omega}, \quad (3)$$

where  $c$  is the speed of light in vacuum. The FDE simulation lists all the modes with their effective refractive indexes and TE fractions. The TE polarization fraction  $f_{E_y}$  for propagation along the  $x$  direction is defined by the following equation:

$$f_{E_y} = \frac{\int |E_y|^2 dydz}{\int (|E_y|^2 + |E_z|^2) dydz}, \quad (4)$$

where  $|E_y|^2 + |E_z|^2$  corresponds to  $|E_{\parallel}|^2$  since we are in consideration of the polarization of the modes, we only think about the fields parallel to the waveguide cross section. To put it simply, the mode is  $E_y$  polarized when  $f_{E_y} = 1$  and the mode is  $E_z$  polarized if  $f_{E_y} = 0$ . The simulation results of effective refractive index and polarization based on 1550 nm wavelength light incidence in terms of varying energies and fluences are tabulated in Table 1. In principle, compared to the refractive index of pristine diamond (2.3878, at 1550 nm wavelength), the greater the effective refractive index  $n_{\text{eff}}$  (mainly referring to the real part as the imaginary part just indicates extinction) one mode has, the more dominant the mode is in the light wave-guiding.

Table 1 shows that all three-energy proton implantations with fluences ranging from  $F_2$  ( $8 \times 10^{15} \text{ cm}^{-2}$ ) to  $F_5$  ( $1.5 \times 10^{16} \text{ cm}^{-2}$ ) support

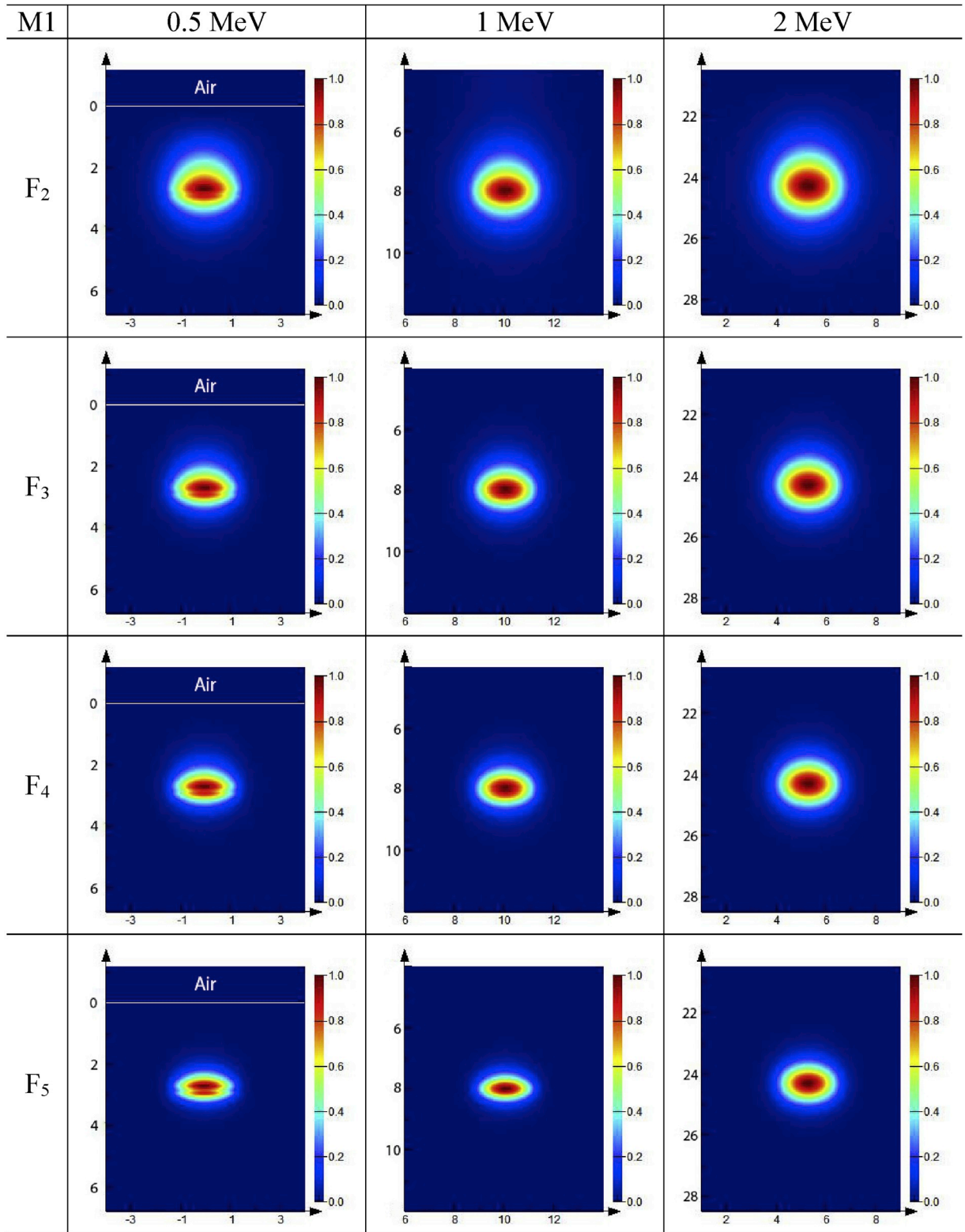


Fig. 3. Mode 1 electric field intensity profiles (2  $\mu\text{m}$  scan width + beam spot size + lateral straggling).

two  $n_{\text{eff}}$ -close waveguide modes (mode 1, mode 2). As a matter of fact, the two  $n_{\text{eff}}$ -close modes essentially indicate one single mode but only with orthogonal polarization directions. This single mode is identified as hybrid mode  $\text{HE}_{11}$  in fiber optics [33], which is the lowest order mode featuring linear polarization that propagates inside an optical fiber. Therefore, all the above-mentioned 12 sets of two  $n_{\text{eff}}$ -close modes

supported waveguide channels can be used for single-mode light wave-guiding. To determine whether horizontal polarization (denoted by  $E_y$ ) or vertical polarization (denoted by  $E_z$ ) is prevailing, one with higher refractive index contrast is labelled as mode 1 while the other is labelled as mode 2. It is worth noting that here mode 1 and mode 2 signify the same mode in nature, such a labelling method is basically used to emphasize the polarization priority.



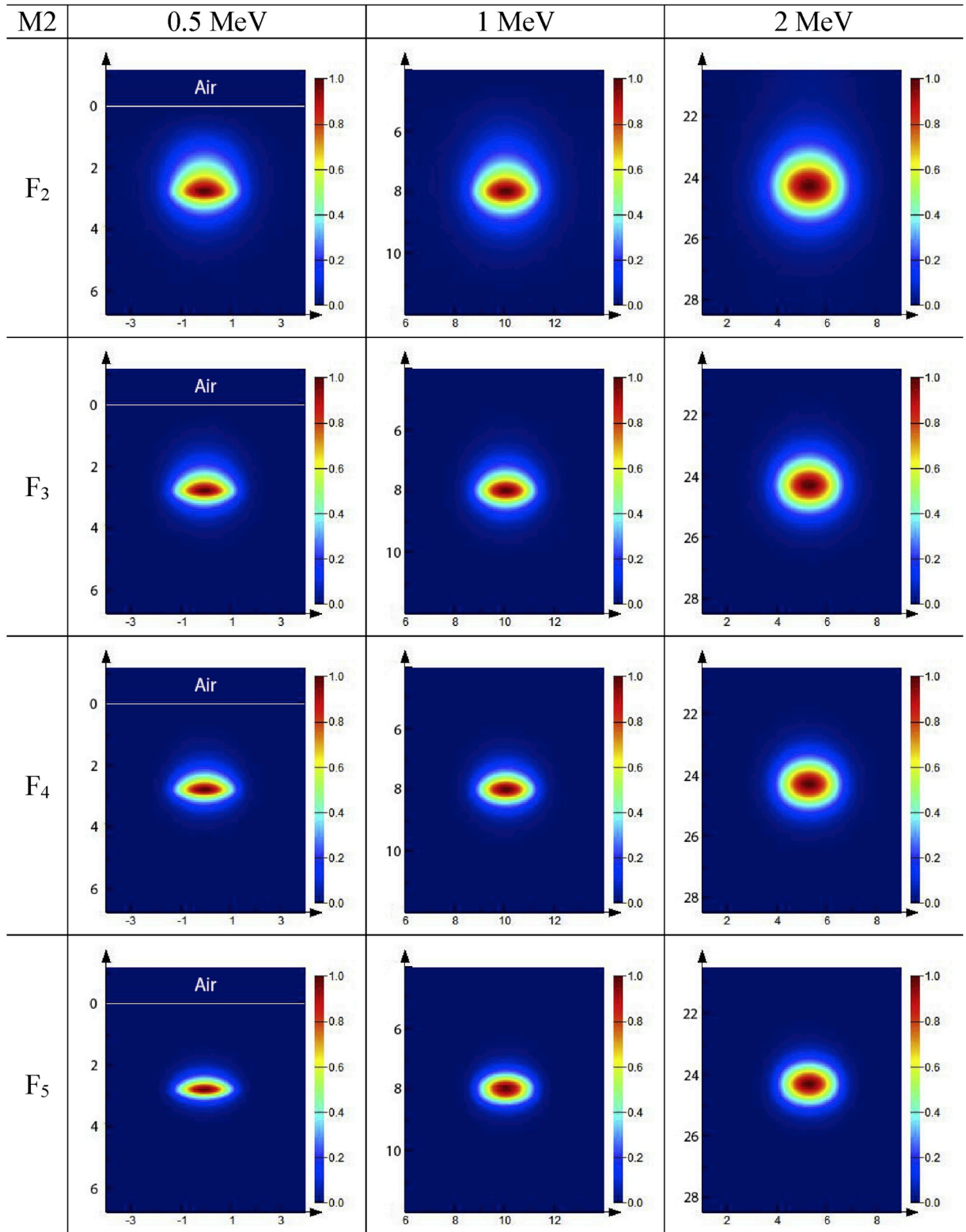


Fig. 4. Mode 2 electric field intensity profiles (2  $\mu\text{m}$  scan width + beam spot size + lateral straggling).

Fig. 3 and Fig. 4 display the electric field intensity profiles of mode 1 (M1) and mode 2 (M2) of the 12 kinds of workable waveguide channels with corresponding configuration parameters shown in Table 1. From Figs. 3 and 4, for each mode we can observe that: 1) at the same energy, the mode spot size becomes smaller with the increase of fluence; 2) at the same fluence, the mode spot size gets larger with increasing energy; 3) at the same energy and the same fluence, there is no much difference

in the mode spot size between mode 1 and mode 2, except that the mode profiles of mode 1 of varying fluences at 0.5 MeV energy are somewhat irregular while those of mode 2 do not reveal such a phenomenon. Apart from that, it is important not to overlook the existence of high order modes. As indicated by mode 3 (M3), mode 4 (M4), mode 5 (M5) in Table 1, waveguide channels made by MeV proton implantations at the fluences  $F_4$  ( $1 \times 10^{16} \text{ cm}^{-2}$ ) and  $F_5$  ( $1.5 \times 10^{16} \text{ cm}^{-2}$ ) show extra modes

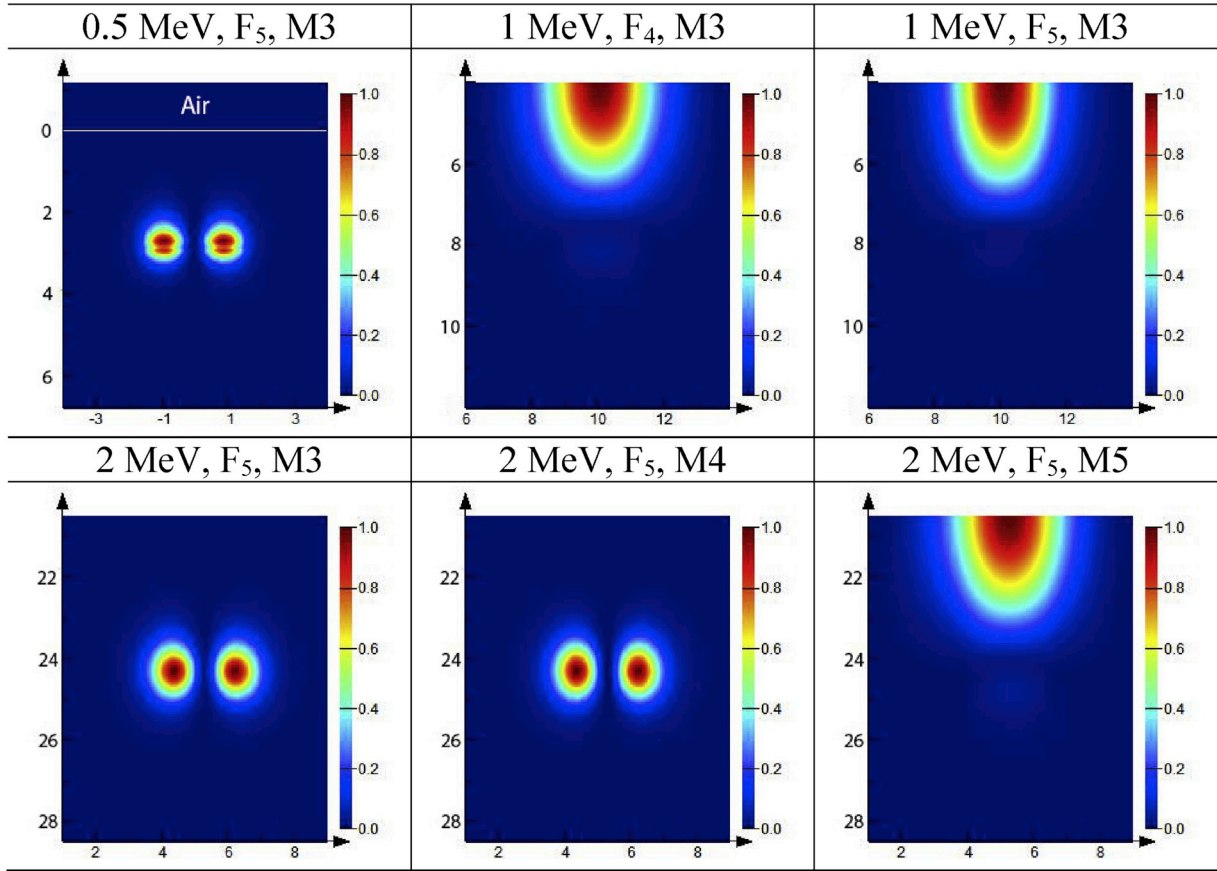


Fig. 5. Higher-order modal electric field intensity profiles (2  $\mu\text{m}$  scan width + beam spot size + lateral straggling).

in addition to their fundamental modes. Furthermore, as shown in Fig. 5, it may be argued that the emerging of some of these high-order modes such as mode 3 (1 MeV,  $F_4$ ), mode 3 (1 MeV,  $F_5$ ) and mode 5 (2 MeV,  $F_5$ ) is mainly attributed to the boundary condition. Strictly speaking, they are not truly accommodated modes. Nevertheless, such a mode is a precursor signal to indicate the appearance of higher-order modes provided that a larger core area or a higher core-cladding refractive index contrast or both are applied. On the other hand, one higher-order mode (i.e. mode 3) appears for 0.5 MeV proton implantation with fluence  $F_5$  ( $1.5 \times 10^{16} \text{ cm}^{-2}$ ), which is perhaps due to high refractive index contrast. Furthermore, the appearance of two extra higher-order modes (M3, M4) for 2 MeV proton implantation with fluence  $F_5$  can be attributed to high refractive index contrast as well as large core area. As we mentioned above, these two modes (i.e. (M3, 2 MeV,  $F_5$ ) and (M4, 2 MeV,  $F_5$ )) virtually indicate the same one but with two perpendicular polarization directions by referring to the effective refractive index and polarization data displayed in Table 1.

### 3. Experimental

The proton beam writing (PBW) facility at the Center for Ion Beam Application (CIBA) in Singapore [34,35] is a state-of-the-art powerful direct-write implantation technique holding tremendous potential for in bulk diamond micro/nano structuring. In this paper, we report three-dimensional single-mode waveguide arrays fabricated in bulk SCD by multi-energy proton beam writing. A sample of type IIa SCD having dimensions of  $0.7 \times 4.0 \times 2.8 \text{ mm}^3$  ( $X \times Y \times Z$ , to keep the same format as that of simulation sections) from Ila Technologies Pte. Ltd. is the original material, and its six facets were polished to optical requirement with a root-mean-square roughness around tens of nanometers. We have fabricated five groups of 3D waveguide arrays with five different

fluences denoted by  $F_1$ ,  $F_2$ ,  $F_3$ ,  $F_4$ , and  $F_5$  as described in the simulation sections (see Table 1). Each group consists of seven spatially separated waveguide channels, every single waveguide channel of each group is 700  $\mu\text{m}$  long, and 2  $\mu\text{m}$  wide (planned scan width). These five groups share the same architecture: two waveguide channels at the bottom, another two waveguide channels in the middle, and the remaining three waveguide channels on the top. The bottom two channels were firstly implanted by 2 MeV proton with a beam current of 34.6 pA; Then the middle two channels were constructed by 2 MeV  $\text{H}_2^+$  (equivalent to 1 MeV proton) with a beam current of 83.7 pA; Finally, the top three channels were formed by 1 MeV  $\text{H}_2^+$  (equivalent to 0.5 MeV proton) implantation with a beam current of 128.6 pA. The measured beam current fluctuation was within  $\pm 5\%$  during our experiments. Before every single implantation of the above-mentioned three, the corresponding proton beams were focused down to about  $300 \times 800 \text{ nm}^2$  (2 MeV proton),  $500 \times 1000 \text{ nm}^2$  (1 MeV proton), and  $900 \times 1600 \text{ nm}^2$  (0.5 MeV proton) under the configuration of object slits opened to  $200 \times 100 \mu\text{m}^2$  and collimator slits opened to  $400 \times 400 \mu\text{m}^2$ . The writing process was done through the combination of beam scanning and stage scanning. Beam scanning was performed in X direction while at the same time stage moving in the perpendicular direction (Y direction). It is worth noting that the directions of X, Y in the PBW experiments are swapped in the simulation sections because X is chosen as propagation direction when performing waveguide simulations for conventionality. Therefore, we only care about the spot size in X direction since stage moves in the Y direction when writing waveguide channels in such a way. Furthermore, the output modes of each group of 3D waveguide arrays were in turn excited by butt coupling a tapered SMF28 fiber (OZ optics, 5  $\mu\text{m}$  spot size (beam waist)) to one entrance facet of the SCD, and the fiber as an input light source was powered by a tunable laser (Agilent 81980A, 1465–1575 nm). The intensity profiles of excited modes were

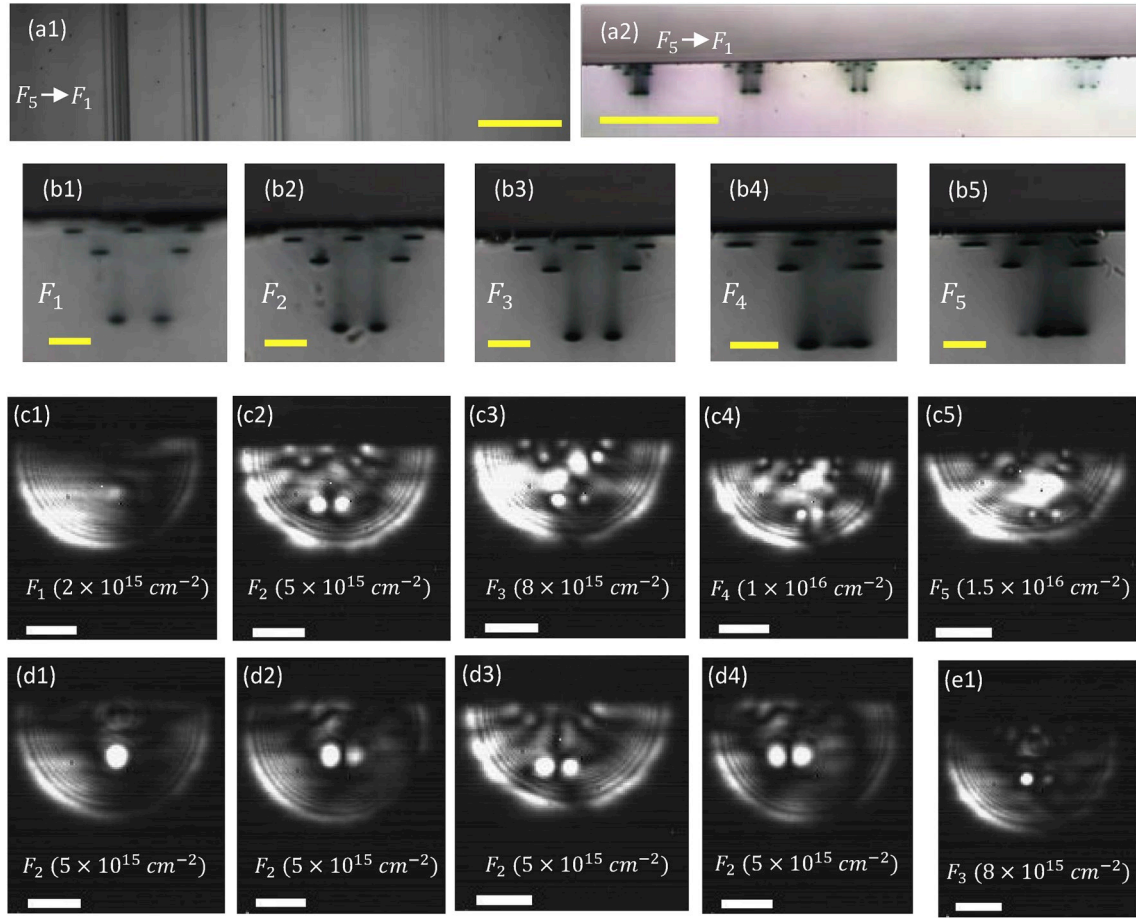


**Fig. 6.** (a1, a2) Optical images of top view and side view of the five groups of the 3D waveguide arrays, respectively. (b1-b5) the fluences  $F_1$ - $F_5$  based waveguide arrays. (c1-c5) InGaAs camera captured images of the light wave-guiding from the exit facet based on the 3D waveguide arrays shown in (b1-b5), respectively. (d1-d4, e1) light wave-guiding scenes based on the 3D waveguide arrays made with fluences  $F_2$  (incoming light shifts from the bottom-left waveguide towards the bottom-right one horizontally, d1-d4) and  $F_3$  (e1), respectively. (Note: the scale bars in yellow in (a1, a2) are 100  $\mu\text{m}$ , in (b1-b5) are 10  $\mu\text{m}$ , and the scale bars in white in (c1-c5, d1-d4, e1) indicate a 20  $\mu\text{m}$  length). (For interpretation of the references to color in this figure legend, the reader is referred to the Web version of this article.)

captured with a cooled InGaAs camera (Xenics Xeva-756) by imaging the other exit facet with a  $60 \times$  (numerical aperture: 0.85) Newport objective.

#### 4. Results and discussion

Fig. 6(a1) is an optical top view image of five groups of waveguide arrays, the maximum fluence  $F_5$  is at the far left while the minimum fluence  $F_1$  is the first from right. There is a 100  $\mu\text{m}$  separation between each two adjacent groups. Fig. 6(a2) is a side view of the output facet of the light wave-guiding. In addition, Fig. 6(b1, b2, b3, b4, b5) present the optical images of the arrays of multi-level waveguide channels with fluences ranging from  $F_1$  to  $F_5$  in the output facet, and it can be observed that the waveguide channels are pretty well-aligned. By varying the relative positions of the input fiber and the diamond sample, incoming single-mode light was defocused and coupled into all seven waveguide channels of each array one by one for five arrays. Fig. 6(c1, c2, c3, c4, c5) are the corresponding concurrent single-mode wave-guiding performance images of the 3D waveguide arrays with fluences ranging from  $F_1$  to  $F_5$ , which were captured by an InGaAs camera located on the exit side of the light wave-guiding of the diamond. Firstly, Fig. 6(c1) indicates that no light guiding was found in the waveguide array with fluence  $F_1$  as predicted in the above-mentioned optical simulations. For the waveguide arrays made with fluences from  $F_2$  to  $F_5$ , Fig. 6(c2, c3, c4, c5) demonstrate that all seven waveguide channels from any group of

these four are capable of achieving light wave-guiding. Generally, the experimental observations from the last four groups ( $F_2$ ,  $F_3$ ,  $F_4$ ,  $F_5$ ) of waveguide arrays are also in agreement with those anticipated from the photonic simulations (see Figs. 3 and 4).

Moreover, it is also of interest to examine a single waveguide channel from a 3D waveguide array. Firstly, based on the 3D waveguide array made with fluence  $F_2$  ( $5 \times 10^{15} \text{ cm}^{-2}$ ), Fig. 6(d1) presents the output image when the bottom-left waveguide channel is intentionally aligned to the input fiber, and a distinct intense light-guiding mode profile can be observed. When shifting the input fiber towards the bottom-right waveguide channel, the evolution images of output scenes over the horizontal displacement are shown in Fig. 6(d2, d3, d4), orderly. In addition, on top of the 3D waveguide array made with fluence  $F_3$  ( $8 \times 10^{15} \text{ cm}^{-2}$ ), it can be seen from Fig. 6(e1) that the bottom-left waveguide channel plays a dominating role in light guiding under a certain coupling configuration (i.e. the input fiber is deliberately coupled to the bottom-left waveguide). Generally, such 3D waveguide arrays can be used as a whole to fabricate complex photonic devices or just be applied as individual waveguide channels depending on the applications.

#### 5. Conclusion

In summary, we have demonstrated the feasibility of designing and fabricating 3D photonic components or devices through the example of the 3D waveguide arrays in bulk diamond theoretically (via simulations)



and experimentally. Single-mode infrared light (1550 nm) wave-guiding in the 3D waveguide arrays made by multi-energy proton implantations in SCD with fluences ranging from  $F_2$  ( $5 \times 10^{15} \text{ cm}^{-2}$ ) to  $F_5$  ( $1.5 \times 10^{16} \text{ cm}^{-2}$ ) was successfully observed. On the other hand, a combination of Monte Carlo based SRIM simulations and Maxwell solver based FDE simulations was also applied, predicting consistent results with those achieved in experiments. It is worth stressing that the 3D waveguide arrays made with fluences  $F_4$  ( $1 \times 10^{16} \text{ cm}^{-2}$ ) and  $F_5$  ( $1.5 \times 10^{16} \text{ cm}^{-2}$ ) are expected to accommodate higher-order modes apart from fundamental modes for MeV proton implantations on the basis of the combined simulations. In addition, these series of simulations can provide an insight into a lower fluence limit (i.e.  $5 \times 10^{15} \text{ cm}^{-2}$ ) and an upper fluence limit (i.e.  $8 \times 10^{15} \text{ cm}^{-2}$ ) of fabricating 3D waveguide arrays for single-mode light wave-guiding. Finally, the demonstrated proton beam writing based implantation technique will open a promising venue for directly fabricating 3D photonic devices in bulk diamond, thus stimulating the development of 3D diamond photonics and color centers based diamond quantum computing.

### Declaration of competing interest

The authors declare that they have no known competing financial interests or personal relationships that could have appeared to influence the work reported in this paper.

### Acknowledgments

Jintao Gong would like to express his gratitude to Dr. Huining Jin for his assistance with light wave-guiding test.

### References

- [1] R. Micheloni, L. Crippa, C. Zambelli, P. Olivo, Architectural and integration options for 3D NAND flash memories, *Computers* 6 (3) (2017) 27.
- [2] H. Liang, S. Vanga, J. Wu, B. Xiong, C. Yang, A. Bettiol, M. Breese, Fabrication of 3D photonic components on bulk crystalline silicon, *Opt. Express* 23 (1) (2015) 121–129.
- [3] D. Wei, C. Wang, H. Wang, X. Hu, D. Wei, X. Fang, Y. Zhang, D. Wu, Y. Hu, J. Li, S. Zhu, M. Xiao, Experimental demonstration of a three-dimensional lithium niobate nonlinear photonic crystal, *Nat. Photonics* 12 (10) (2018) 596.
- [4] I. Aharonovich, A.D. Greentree, S. Praver, Diamond photonics, *Nat. Photonics* 5 (7) (2011) 397.
- [5] A.M. Zaitsev, *Optical properties of diamond: a data handbook*, Springer Science & Business Media, 2013.
- [6] V. Bharadwaj, O. Jedrkiewicz, J.P. Hadden, B. Sotillo, M.R. Vázquez, P. Dentella, T. Fernandez, A. Chiappini, A.N. Giakoumaki, T.L. Phu, M. Bollani, M. Ferrari, R. Ramponi, P.E. Barclay, S.M. Eaton, Femtosecond laser written photonic and microfluidic circuits in diamond, *J. Phys.: Photonics* 1 (2) (2019) 022001.
- [7] M.K. Bhaskar, D.D. Sukachev, A. Sipahigil, R.E. Evans, M.J. Burek, C.T. Nguyen, L. J. Rogers, P. Siyushev, M.H. Metsch, H. Park, et al., Quantum nonlinear optics with a germanium-vacancy color center in a nanoscale diamond waveguide, *Phys. Rev. Lett.* 118 (22) (2017) 223603.
- [8] S. Praver, A.D. Greentree, Diamond for quantum computing, *Science* 320 (5883) (2008) 1601–1602.
- [9] P.C. Maurer, G. Kucsko, C. Latta, L. Jiang, N.Y. Yao, S.D. Bennett, F. Pastawski, D. Hunger, N. Chisholm, M. Markham, D.J. Twitchen, J.I. Cirac, M.D. Lukin, Room-temperature quantum bit memory exceeding one second, *Science* 336 (6086) (2012) 1283–1286.
- [10] S.M. Eaton, J.P. Hadden, V. Bharadwaj, J. Forneris, F. Piccolo, F. Bosia, B. Sotillo, A.N. Giakoumaki, O. Jedrkiewicz, A. Chiappini, M. Ferrari, R. Osellame, P. E. Barclay, P. Olivero, R. Ramponi, Quantum micro–nano devices fabricated in diamond by femtosecond laser and ion irradiation, *Adv. Quantum Technol.* (2019) 1900006.
- [11] P. Latawiec, V. Venkataraman, M.J. Burek, B.J. Hausmann, I. Bulu, M. Lončar, On-chip diamond Raman laser, *Optica* 2 (11) (2015) 924–928.
- [12] T.M. Babinec, J.T. Choy, K.J. Smith, M. Khan, M. Lončar, Design and focused ion beam fabrication of single crystal diamond nanobeam cavities, *J. Vac. Sci. Technol. B Nanotechnol. Microelectron.: Mater. Process. Meas. Phenom.* 29 (1) (2011) 010601.
- [13] B. Khanaliloo, M. Mitchell, A.C. Hryciw, P.E. Barclay, High-q/v monolithic diamond microdisks fabricated with quasi-isotropic etching, *Nano Lett.* 15 (8) (2015) 5131–5136.
- [14] B. Sotillo, V. Bharadwaj, J. Hadden, M. Sakakura, A. Chiappini, T.T. Fernandez, S. Longhi, O. Jedrkiewicz, Y. Shimotsuma, L. Criante, R. Osellame, G. Galzerano, M. Ferrari, K. Miura, R. Ramponi, P.E. Barclay, S.M. Eaton, Diamond photonics platform enabled by femtosecond laser writing, *Sci. Rep.* 6 (2016) 35566.
- [15] V. Bharadwaj, A. Courvoisier, T. Fernandez, R. Ramponi, G. Galzerano, J. Nunn, M. Booth, R. Osellame, S. Eaton, P. Salter, Femtosecond laser inscription of Bragg grating waveguides in bulk diamond, *Opt. Lett.* 42 (17) (2017) 3451–3453.
- [16] M.J. Burek, N.P. de Leon, B.J. Shields, B.J. Hausmann, Y. Chu, Q. Quan, A. S. Zibrov, H. Park, M.D. Lukin, M. Lončar, Free-standing mechanical and photonic nanostructures in single-crystal diamond, *Nano Lett.* 12 (12) (2012) 6084–6089.
- [17] F. Watt, M.B. Breese, A.A. Bettiol, J.A. van Kan, Proton beam writing, *Mater. Today* 10 (6) (2007) 20–29.
- [18] J. Forneris, V. Grilj, M. Jakšić, A.L. Giudice, P. Olivero, F. Piccolo, N. Skukan, C. Verona, G. Verona-Rinati, E. Vittone, IBIC characterization of an ion-beam-micromachined multi-electrode diamond detector, *Nucl. Instrum. Methods Phys. Res. Sect. B Beam Interact. Mater. Atoms* 306 (2013) 181–185.
- [19] P. Olivero, J. Forneris, M. Jakšić, Ž. Pastuović, F. Piccolo, N. Skukan, E. Vittone, Focused ion beam fabrication and IBIC characterization of a diamond detector with buried electrodes, *Nucl. Instrum. Methods Phys. Res. Sect. B Beam Interact. Mater. Atoms* 269 (20) (2011) 2340–2344.
- [20] A. Karabutov, V. Ralchenko, I. Vlasov, R. Khmel'nitsky, M. Negodaev, V. Varnin, I. Teremetskaya, Surface engineering of diamond tips for improved field electron emission, *Diam. Relat. Mater.* 10 (12) (2001) 2178–2183.
- [21] P. Sellin, A. Galbiati, Performance of a diamond X-ray sensor fabricated with metal-less graphitic contacts, *Appl. Phys. Lett.* 87 (9) (2005) 93502.
- [22] S. Lagomarsino, P. Olivero, F. Bosia, M. Vannoni, S. Calusi, L. Giuntini, M. Massi, Evidence of light guiding in ion-implanted diamond, *Phys. Rev. Lett.* 105 (23) (2010) 233903.
- [23] S. Lagomarsino, S. Calusi, M. Massi, N. Gelli, S. Sciortino, F. Taccetti, L. Giuntini, A. Sordini, M. Vannoni, F. Bosia, D.G. Monticone, P. Olivero, B.A. Fairchild, P. Kashyap, A.D.C. Alves, M.A. Strack, S. Praver, A.D. Greentree, Refractive index variation in a free-standing diamond thin film induced by irradiation with fully transmitted high-energy protons, *Sci. Rep.* 7 (1) (2017) 385.
- [24] H. Jin, S.P. Turaga, S.K. Vanga, A.A. Bettiol, Single-mode light guiding in diamond waveguides directly written by a focused proton beam, *Opt. Lett.* 43 (11) (2018) 2648–2651.
- [25] J.F. Ziegler, M.D. Ziegler, J.P. Biersack, SRIM—the stopping and range of ions in matter (2010), *Nucl. Instrum. Methods Phys. Res. Sect. B Beam Interact. Mater. Atoms* 268 (11–12) (2010) 1818–1823.
- [26] J. Bourgoïn, B. Massarani, Threshold energy for atomic displacement in diamond, *Phys. Rev. B* 14 (8) (1976) 3690.
- [27] R. Silva, S. Silva, Properties of amorphous carbon, 2003 no. 29, Iet.
- [28] Z. Zhu, T.G. Brown, Full-vectorial finite-difference analysis of microstructured optical fibers, *Opt. Express* 10 (17) (2002) 853–864.
- [29] M.N. Polyanskiy, Refractive index database. <https://refractiveindex.info> accessed on 2019-09-20.
- [30] S. Lagomarsino, P. Olivero, S. Calusi, D.G. Monticone, L. Giuntini, M. Massi, S. Sciortino, A. Sytchkova, A. Sordini, M. Vannoni, Complex refractive index variation in proton-damaged diamond, *Opt. Express* 20 (17) (2012) 19382–19394.
- [31] P. Olivero, S. Calusi, L. Giuntini, S. Lagomarsino, A.L. Giudice, M. Massi, S. Sciortino, M. Vannoni, E. Vittone, Controlled variation of the refractive index in ion-damaged diamond, *Diam. Relat. Mater.* 19 (5–6) (2010) 428–431.
- [32] A. Battiatto, F. Bosia, S. Ferrari, P. Olivero, A. Sytchkova, E. Vittone, Spectroscopic measurement of the refractive index of ion-implanted diamond, *Opt. Lett.* 37 (4) (2012) 671–673.
- [33] A.W. Snyder, R.A. Sammut, Fundamental ( $HE_{11}$ ) modes of graded optical fibers, *JOSA* 69 (12) (1979) 1663–1671.
- [34] J. Van Kan, P. Malar, A. Baysic de Vera, The second generation Singapore high resolution proton beam writing facility, *Rev. Sci. Instrum.* 83 (2) (2012), 02B902.
- [35] Y. Yao, J. Van Kan, Automatic beam focusing in the 2nd generation PBW line at sub-10 nm line resolution, *Nucl. Instrum. Methods Phys. Res. Sect. B Beam Interact. Mater. Atoms* 348 (2015) 203–208.